Research Square

Preprints are preliminary reports that have not undergone peer review.
They should not be considered conclusive, used to inform clinical practice,
or referenced by the media as validated information.

Optimized Design of Liquid Hydrogen Turbo-Pump for Heavy-Lift Class Rocket

Jishnu Kunal Vutukuru
Manipal Academy of Higher Education
Kaushik Iyer
Manipal Academy of Higher Education
Santhosh Karthikeyan
Manipal Academy of Higher Education
Raghunandana K
raghu.bhat@manipal.edu

Manipal Academy of Higher Education

Research Article

Keywords: High Entropy Alloys, Fluid Structure Interaction, Impeller, Modal Analysis, Parametric Blade Design

Posted Date: November 19th, 2026

DOI: https://doi.org/10.21203/rs.3.rs-11621340/v1

License: This work is licensed under a Creative Commons Attribution 4.0 International License.
Read Full License

Additional Declarations: No competing interests reported.

Optimized Design of Liquid Hydrogen Turbo-Pump for Heavy-Lift Class Rocket

Jishnu Kunal Vutukuru, Kaushik Iyer, Santhosh Karthikeyan, Raghunandana K*
Manipal Institute of Technology, Manipal Academy of Higher Education, Manipal.
* Corresponding Author: raghu.bhat@manipal.edu

Abstract:

Liquid hydrogen (LH_2) turbopumps operate under extreme thermofluidic and mechanical loading conditions, including cryogenic temperatures, high rotational speeds, and cavitation-prone flow regimes, placing stringent demands on both aerodynamic performance and structural integrity. This study presents an integrated computational workflow for designing and evaluating a cryogenic centrifugal impeller, combining parametric blade geometry generation, steady-state computational fluid dynamics (CFD), one-way fluid–structure interaction (FSI), and modal analysis. An in-house Python routine was used to generate optimized blade geometry, which was subsequently modelled in ANSYS BladeGen, meshed in ANSYS TurboGrid, and analysed under LH_2 operating conditions (44.9 kg/s mass flow rate, 91 bar outlet pressure) using ANSYS CFX. Resulting pressure and thermal loads were mapped onto a structural finite element model in ANSYS Mechanical to assess stress, deformation, and dynamic stability across seven candidate materials: Inconel 718, four high-entropy/medium-entropy alloys (HEAs/MEAs), and two Al6061-based metal matrix composites (B_4C- and SiC-reinforced). The CFD analysis confirmed target performance, achieving an outlet pressure of 91.2 bar and a hydraulic efficiency of 0.939. FSI results showed all candidate materials remained within acceptable elastic limits, with the Al6061 + SiC composite exhibiting the lowest stress (118 MPa) and the CoCrFeMnNi HEA showing superior stiffness-to-weight characteristics. Modal analysis confirmed that natural frequencies for all materials avoided the pump's operating speed range, ensuring resonance-free operation. These findings demonstrate that HEAs and particle-reinforced MMCs are viable, lightweight alternatives to conventional nickel-based superalloys for next-generation cryogenic turbomachinery, offering pathways toward more efficient and cost-effective LH_2 propulsion hardware.

Keywords: High Entropy Alloys, Fluid Structure Interaction, Impeller, Modal Analysis, Parametric Blade Design.

Abbreviations:

Abbreviation	Expansion
AA	Aluminium Association (alloy designation prefix, e.g., AA2195, AA2219, AA6061)
AlN	Aluminium Nitride
AMC	Aluminium Matrix Composite
B_4C	Boron Carbide
BCC	Body-Centred Cubic
CFD	Computational Fluid Dynamics
CTE	Coefficient of Thermal Expansion
DTBT	Ductile-to-Brittle Transition
ELI	Extra Low Interstitial
FCC	Face-Centred Cubic
FSI	Fluid–Structure Interaction
HCF	High-Cycle Fatigue
HEA	High-Entropy Alloy
LH_2	Liquid Hydrogen
LNT	Liquid Nitrogen Temperature
LOX	Liquid Oxygen
MEA	Medium-Entropy Alloy
MFGF	Mass Flow Gain Factor
MMC	Metal Matrix Composite
NBP	Normal Boiling Point
NPSH	Net Positive Suction Head
NS	Specific Speed
RANS	Reynolds-Averaged Navier–Stokes

rpm	Revolutions per Minute
RT	Room Temperature
SFE	Stacking Fault Energy
SiC	Silicon Carbide
SSS	Suction Specific Speed
SST	Shear Stress Transport (turbulence model)
UTS	Ultimate Tensile Strength
wt%	Weight Percent

1. Introduction

Turbopumps make up an essential component in high-performance fluid systems, specifically in the field of aerospace propulsion, cryogenic systems, and power generation. At its core, a turbopump brings together a pump and a turbine to increase the inlet pressure of a fluid while ensuring higher mass flow rates. Key components of a turbopump are the inducer, impeller, diffuser, and volute casing.

At the core of a turbopump is the impeller, which transfers rotational energy from the driveshaft into the working fluid. The shape and configuration of an impeller (radial, axial, or mixed flow), as well as the thickness and surface finish, can be a key factor in determining the performance of the turbopump.

1.1 Properties of Liquid Hydrogen:

Table 1 summarizes the thermophysical properties of liquid hydrogen. Hydrogen-fuelled cryogenic propulsion requires turbopump hardware that must balance extreme thermofluidic environments against aggressive mechanical loads. Liquid hydrogen has a very low density of $\approx 70\ kg \cdot m^{-3}$ and a boiling point of $\approx -253\ °C$ at 1 atm, driving liquid-to-gas expansion ratios to enormous values (~1:848) and causing thermophysical effects that alter cavitation dynamics compared to conventional fluids. Within high-performance engines, such as the Vulcain class, LE-5, or 50k lbf-class designs, LH_2 turbopumps rotate at tens of thousands of rpm with severe pressure rises while sustaining high tip speeds.[1] LH_2 also benefits from thermodynamic suppression of cavitation due to the fluid's specific heat and vapor pressure characteristics, translating into lower Net Positive Suction Head (NPSH) requirements compared with water in most operating regimes. The underlying reason behind this is thermodynamic suppression, or the collapsing/suppression of vapor cavities because of the rapid heat transfer between the fluid and surroundings, which becomes significant in LH_2 pumps. This allows much lower cavitation numbers σ and higher NPSH performance.[1] The impact on NPSH has be quantified to find that ≈32 m was required for LH_2 compared to 63 m for water in a controlled experiment, proving the advantageous suction margin of LH_2.[2] All these relevant properties of LH2 that affect the operating parameters of a turbopump and also set the requirements for the material selection for the same applications have been tabulated below in Table 1.

Table 1 Thermophysical Properties of LH2 [2], [3]

Property	Symbol	Value at NBP (20.3 K)	Units	Significance to pump design
Density (liquid)	ρL	70.85	kg/m³	Sets impeller tip speed and head requirements
Vapor pressure	pv	101.3 (1 atm)	kPa	Determines NPSH requirement; very sensitive to T
Dynamic viscosity (liquid)	μ	13.2	μPa·s	~75× lower than water → very high Re; affects leakage flows
Thermal conductivity	k	0.099	W/(m·K)	Low k means thermal gradients persist; important for heat-in leak
Latent heat of vaporization	hfg	445.3	kJ/kg	Drives thermodynamic cavitation suppression (B-factor)
Specific heat capacity (liquid)	cp,L	9.69	kJ/(kg·K)	Governs temperature recovery in cavitation; high cp beneficial
Surface tension	γ	1.92	mN/m	Very low surface tension makes bubble nucleation easier
Density ratio ρL/ρv	ρL/ρv	~65 at 20.3 K	–	Low ratio amplifies thermodynamic suppression; cavity less dense than in water

1.2 LH_2 Fluid Properties and Thermodynamic/Cavitation Implications

Swept-back, low-loading inducer geometries have been shown to significantly reduce cavitation inception and tip vortex strength.[4] Blade loading in optimized LH_2 inducers is usually within the range of 0.8–1.2 MPa/m, a balance between hydraulic performance and the associated risks for cavitation.

Unstable cavitating behaviour can be triggered by backflow at the impeller inlet. It has been shown that MFGF values of 0.1- 0.3 and a critical $\sigma \approx 0.1285$ correspond to cavity-volume minima.[5] This suggests that inducer and hub geometry should be tuned to minimize inlet backflow and to damp any instabilities related to MFGF. In practical pump

design, this calls for attention to inducer leading-edge geometry, inlet fillets, and hub contours.

Researchers have performed both experimental non-cavitation tests and numerical cryogenic simulations of an LOX turbopump, finding that thermodynamic effects in LOX shift the suction-side pressure distribution relative to water tests, with the gap leakage vortex intensity strongly dependent on both rotating speed and fluid thermodynamic properties.[6] The paper quantified turbopump performance variation across a 40% speed range (60–100% of design speed). Cavitation collapse near blade surfaces may cause micro-pitting, erosion, and early crack nucleation. Although LH_2 has thermodynamic suppression effects, cavitation can be considered the primary concern under off-design conditions and at the inducer or inducer-blade interactions.

LH_2 service may have a risk of hydrogen diffusion, trapping, and embrittlement for susceptible materials. Materials with FCC microstructures-e.g., many austenitic steels, certain HEAs, some Al alloys-maintain ductility at low temperatures and are less susceptible to brittle fracture; phases dominated by BCC structures are more resistant to embrittlement or DTBT[7], [8]

High rpm operation implies very high cycle counts per mission. Coupled thermo-mechanical loads-for example, differential contraction between hub and blades, frequent thermal ramps-can accelerate fatigue crack initiation. Surface quality, microstructure, residual stresses from manufacturing, and notch sensitivity will play the dominant roles in controlling fatigue life under the cryogenic HCF regimes.

Stress concentrations, cavitation, and dynamic excitation hot spots are at the blade roots, dovetails, and fillets. Cavitation erosion can locally reduce cross-section and create initiation sites; rotor imbalances create alternating bending and torsion on blades. Safety margins and inspections, therefore, must assume multi-mechanism fatigue initiation.

1.3 Dimensionless numbers and scaling

Dimensionless groups are indispensable for scaling turbopump performance.

Flow coefficient (φ): generally, 0.03–0.15 for LH_2 inducer applications;[1] shows $\varphi \approx 0.03$–0.05 in early swept-back inducer tests.

Cavitation number σ: LH_2 experiments obtain σ as low as 0.001 – 0.01 experimentally [1], [9], while CFD threshold studies in such conditions indicate critical $\sigma \approx 0.1285$ for cavity volume minima in some regimes.

Specific speed (NS) and Suction Specific Speed (SSS): A 50k lbf pump was designed with NS ≈ 17,000 (a high specific speed regime for cryogenic turbopumps).[10] SSS reached 300,000 in successful designs. [1]

These nondimensional scaling laws govern the translation of lab data, including water analogues and small-scale rigs, to flight-scale turbopumps.

1.4 Extensive Review of Materials: Conventional Alloys, Composites, and HEAs

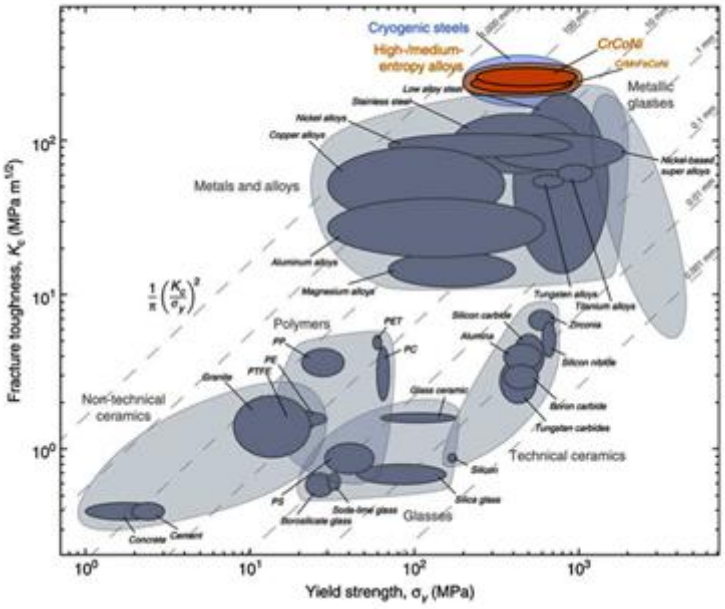


Figure 1. Fracture Toughness of Materials [8]

1.4.1 Material Properties for potential cryogenic turbopump applications

Figure 1 shows that HEAs have strong potential for turbomachinery applications because they offer a unique combination of high yield strength and fracture toughness. Similarly, Titanium alloys, Aluminium Matrix Composites, as well as nickel-based superalloys have been studied for their favourable properties. Compiled below is an extensive review of the materials and the related fabrication processes to gauge their feasibility for cryogenic turbopump applications.

Aluminium Alloys & Reinforced Aluminium Matrix Composites (AMCs/MMCs): Al 6061 has been employed in several historical turbopump impellers, such as the LE-5 documentation. This alloy has good manufacturability, coupled with acceptable cryogenic toughness.

A356.0-T6 also shows consistent toughness down to 77K without DTBT and thus is suitable for cryogenic structural parts [11]. Besides, this alloy is also widely used for casings that call for cast geometry and light weight [12].

The High-strength Al-Cu and Al-Li alloys, such as AA2219/AA2195, have demonstrated various improvements in cryogenic performance. AA2219 is used for impellers in several designs.[13] Reducing temperature below ambient leads to higher tensile and yield strengths in the case of AA2195, which shows increased resistance while retaining appreciable ductility. Aluminium alloys demonstrate excellent specific stiffness and low density, which should be beneficial in minimizing centrifugal loading. However, pure aluminium alloys may have lower bulk modulus and limited fatigue strength compared to titanium or HEAs under extremely high RPM loads.

SiC & B_4C reinforcement: Studies on SiC and B_4C-reinforced aluminium matrix composites report considerable yield/UTS increases at cryogenic temperatures and enhancement of strain hardening because of the thermal mismatch stresses and dislocation storage. Some studies present progressive strength increases in SiC-reinforced Al composites with the reduction of temperature down to 77 K and enhanced fracture toughness.[14],[4]

AlN reinforcement: AlN-reinforced Al-Mg matrices [15] showed a gain of up to 90% improvement in yield/UTS at LNT, with Al-5Mg/AlN reaching ≈61 MPa (LNT), although contrasted with reduced elongation. The morphology of AlN particles and good lattice compatibility reduce crack concentration risk compared to sharp ceramic particulates.

B_4C particle/boron fiber reinforcement: Boron-fiber-reinforced Al alloys developed maximum yield strength ≈1350 MPa at 77 K, but their strength fell at 4.2 K; this non-monotonicity suggests that for some composites, optimal cryogenic temperature windows may exist [14].

From this it is evident that reinforced Al MMCs have high specific strength, higher dynamic stiffness (resonant frequency improvements ≈ 70% reported), and lower CTE, highly attractive for LH_2 impellers where mass savings reduce centrifugal loads. The fatigue crack initiation behaviour at the particle-matrix interface in HCF regimes needs explicit characterization.

Titanium Alloys (Ti-5Al-2.5Sn ELI, Ti-6Al-4V): Ti-5Al-2.5Sn (alpha alloy) and Ti-6Al-4V (alpha-beta) have twice as high yield and tensile strength at cryogenic temperatures (4.2 K) but a considerable loss of elongation (~1/3 of RT). On the other hand, Ti-5Al-2.5Sn retains much better fracture toughness and is therefore preferred for cryogenic rotor blades.[16]

Titanium alloys are the established standard in aerospace rotorcraft and cryogenic pump applications. Titanium provides excellent strength/weight and acceptable fatigue properties with proper surface finishing and heat treatment. Limitations of implementing Ti alloys include cost, machining difficulty, and the potential for ignition in LOX environments; these would have to be dealt with at the design level [13].

Based on specific strength and fracture toughness, the Ti alloys are a strong candidate for LH_2 impellers. Regardless, more detailed fatigue testing of HCF at operational rpm will be required to better determine their actual performance capabilities in LH2 pump applications.

For Ti and Al alloys, conventional machining remains standard, but attention to surface finish and residual stress control is mandatory to maximize fatigue life.

Silver coatings are used historically to prevent reactivity issues such as Ti in LOX contexts and reduce ignition risk. [17] Surface finishing such as polishing and shot peening can dramatically affect fatigue initiation thresholds; shot peening/laser peening may be challenging on composite surfaces.

Nickel-Base Superalloys (Inconel 718): Inconel 718 finds wide applications in high-temperature and cryogenic components. It shows excellent strength stability and fatigue resistance, while its high density is considered a drawback in rotating parts where mass is considered critical [13].

Many turbomachine casings and hot-section parts are made of Inconel; impellers for LH_2 service seldom employ high-density nickel alloys unless mass is accepted for the required life. These alloys are found to be useful in hubs or components where strength is important, and mass is secondary, or when manufacturing issues favour Inconel. Not preferred for high-rpm impeller blades where density penalizes centrifugal stresses.

High-Entropy Alloys (HEAs) & Medium-Entropy Alloys (MEAs): HEAs often combine surprising combinations of strength, ductility, and fracture toughness at cryogenic temperatures. Recent studies have shown that FCC HEAs preserve ductility and fracture toughness even at cryogenic temperatures [7], [8], [18].

In the single-phase FCC HEAs (for example, CrCoNi), exceptionally high fracture toughness and strain hardening with twinning-assisted plasticity at low T have been realized, resulting in high toughness with balanced ductility. The yield strengths reported in the cryogenic regime are variable; e.g., CoCrFeMnNi has strengths of ~310-436 MPa as a function of grain size.[18] TiZrHfNbTa has a reported yield strength ≈1549 MPa at 77 K with ductility ≈20.8% and no evident DTBT.[18] The strengthening arises from multiple mechanisms such as dislocation activity, twinning, and deformation-induced phase transformations.

Some of the Al-containing HEAs & BCC-rich HEAs, such as AlCoCrFeNi, represent enhanced strength at 77 K but tend towards low toughness if the fraction of BCC is high [7], [19].

SFE controls the dominant deformation mode. Low SFE enables toughness, enhances work hardening through partial dislocation separation, deformation twinning, and martensitic

transitions that impede necking at low temperatures [18]. For cryogenic impellers, HEAs with low SFE and FCC microstructure (minimised BCC fraction) are therefore attractive as this structure combines toughness, ductility, and strength; on the other hand, BCC-rich HEAs can be brittle due to high triaxial stresses imposed on them [7].

The high-cycle fatigue performance at ultra-high rpm is less established in the HEA literature. Dedicated HCF testing and S–N curve generation at cryogenic temperatures are needed to properly gauge the applicability of HEAs in LH2 rotors.

Early indications are that some HEAs resist hydrogen embrittlement; explicit hydrogen permeation/embrittlement studies in LH_2 service are limited.

Therefore, HEAs are a frontier that could offer transformative mechanical advantages for cryogenic impellers, provided the cost, manufacturability, and adequate fatigue/hydrogen embrittlement testing are accomplished.

1.4.2 Manufacturing, Joining, Surface Treatment & Coatings

Stir casting and powder metallurgy produce particle-reinforced matrices but require careful control of particle dispersion and porosity [20]. Lately, additive manufacturing has been increasingly used to manufacture geometrical impellers of complicated design as well as for integrated cooling/fillet features. Additive manufacturing of HEAs and MMCs is an active research domain. However, such processes must be critically controlled by process parameters to avoid defects and to result in desired microstructures.

From the perspective of fabrication, it was observed that ultrasonic soldering and composite welding techniques could form strong joints with SiC-reinforced Al composites.[15] The primary routes for particle-reinforced MMCS are stir-casting and powder metallurgy. However, defects, particle clustering, and interface bonding are critical to fatigue life. Ultrasonic soldering for SiC-reinforced composites produced composite welds where mechanical integrity is transferred into joints [17]. Joints between dissimilar materials (e.g., Ti hub to Al blade) need transitional design or mechanical joining to avoid differential CTE stresses and galvanic corrosion.

While they have attractive properties for cryogenic applications, HEAs are expensive and difficult to fabricate into thin, accurate blade geometries, with each of the casting, wrought, and additive manufacturing routes having its own particular microstructural controls.

1.5 Governing Equations

1.5.1 Euler Turbomachinery Equation:

Euler's turbomachinery equation gives the theoretical head delivered by the impeller, derived from the momentum of a control volume between the inducer and impeller exits.

$\Delta H_{Euler} = (U_2 C_{u2} - U_1 C_{u1})/g$ (1)

where U_1, U_2 are blade speeds at inlet and outlet diameters, and C_{u1}, C_{u2} are the absolute tangential (whirl) velocity components. [21], [22]

1.5.2 Continuity Equation:

For incompressible (sub-cavitation) cryogenic flow through the impeller passage [23]:

$$\nabla \cdot (C) = 0 \implies Q = A_1 C_{m1} = A_2 C_{m2} \quad (2)$$

Where A_1 and A_2 are the flow areas at the inlet and outlet, accounting for blade blockage, and C_{m1} and C_{m2} are the mean fluid velocities perpendicular to those cross sections.

1.5.3 Blade Geometry Parameters:

Derived quantities include volumetric flow rate Q_v and angular velocity ω [25]

$$Q_v = \frac{\dot{m}}{\rho} \quad and \quad \omega = \frac{2\,\pi\,N}{60} \quad (3)$$

The blade tip speed U_2, tangential velocity $V_{\theta 2}$, and radial velocity V_{r2} are computed as [24]:

$$U_2 = \omega\, r_2\,; \; V_{\theta 2} = \frac{\nabla P}{\rho U_2}\,; \quad V_{r2} = \frac{Q_v}{2\pi r_2 b_2} \quad (4)$$

The blade outlet angle β_2 is derived from velocity components [23]:

$$\beta_2 = arctan\left(\frac{V_{r2}}{U_2 - V_{\theta 2}}\right) \quad (5)$$

Additional geometric parameters, including blade chord, thickness, leading-edge radius, and number of blades, Z, were calculated using empirical correlations [21], [22], [24]:

$$chord = chord\ to\ height\ ratio * b_2\,, \qquad Z \approx \frac{2\pi r_{mean}\sigma_{target}}{chord} \quad (6)$$

1.5.4 Navier-Stokes Equations (RANS):

The three-dimensional Reynolds-Averaged Navier-Stokes (RANS) equations in a rotating reference frame govern the relative flow field in the impeller [26]. In tensor form:

$$\frac{\partial(\rho W_i)}{\partial t} + \frac{\partial(\rho W_i W_j)}{\partial x_j} = -\frac{\partial p^*}{\partial x_i} + \frac{\partial \tau_{ij}}{\partial x_j} + \rho f_{i,cor} \qquad (7)$$

where W is the relative velocity, p* is the rothalpy-corrected pressure incorporating centrifugal effects, τ_{ij} is the Reynolds stress tensor (closed by SST k-ω or k-ε turbulence models), and $f_{i,cor}$ represents Coriolis body forces. The energy equation must be added when thermodynamic effects are significant, as in cryogenic cavitation.

2. Methodology

The design and analysis of the cryogenic impeller followed a sequential computational workflow. The process began with the Vulcain 2 LH_2 operating point, followed by parametric blade generation in Python, three-dimensional modelling in ANSYS BladeGen, mesh generation and steady-state CFD in ANSYS TurboGrid and CFX, one-way fluid–structure interaction in ANSYS Mechanical, modal analysis, and comparative material assessment. The workflow connected the hydraulic, structural, and dynamic requirements of a single impeller stage rather than treating each analysis in isolation.

2.1 Design basis and operating conditions

The pump was sized against the Vulcain 2 LH_2 turbopump benchmark summarized in Table 2. The reference pump is a two-stage machine with a total pressure rise of 182 bar at a mass flow rate of 44.9 kg/s and a rotational speed of 35,800 rpm. The impeller studied here represents one stage and was therefore designed for a nominal pressure rise of 91 bar. At approximately 20 K, the LH_2 density was taken as 70.85 kg/m³, giving a volumetric flow rate of about 0.634 m³/s. The corresponding angular velocity is 3,749 rad/s, and the shaft operating frequency is approximately 597 Hz. This frequency was used as the primary reference in the modal assessment.

Table 2. Two-stage pump characteristics of the Vulcain 2 LH_2 turbopump [25]

LH_2 Turbopump	
Pump Mass flow (kg/s)	44.9
Pump head rise (bar)	182
Pump rotational speed (rpm)	35800
Turbine mass flow (kg/s)	6.0
Power (MW)	14.5

2.2 Parametric blade geometry generation

The preliminary impeller geometry was generated with an in-house Python program. The code accepts mass flow rate, fluid density, rotational speed, and per-stage pressure rise as inputs and checks that the values are physically meaningful before starting the design sweep. Its logic is shown in Figure 2.

For each candidate tip radius r_2, the program calculated the blade tip speed and estimated the outlet tangential velocity required to meet the stage pressure target. Candidates for which the required tangential velocity approached the blade speed were rejected because they would imply an impractical velocity triangle. For each outlet blade height b_2, the radial velocity and flow coefficient were then calculated, followed by the outlet relative flow angle β_2.

The blade chord was set as $1.2b_2$. Thickness, leading-edge radius, and trailing-edge dimensions were defined as fixed fractions of the chord, while the suggested blade count was obtained from a target solidity evaluated at 70% of the tip radius. The sweep covered tip radii of 0.08–0.12 m, blade heights of 0.07–0.09 m, and hub-to-tip ratios of 0.40, 0.45, and 0.50, giving 45 candidate combinations. Candidates were screened to retain four to eight blades and then ranked by outlet blade angle. The final geometry was selected after checking the pressure-rise target, blade-count constraint, and feasibility of the velocity triangle.

2.3 Meshing and mesh independence

The impeller was meshed in ANSYS TurboGrid with a structured hexahedral mesh and near-wall refinement to resolve the boundary layer. Mesh quality was monitored using skewness and aspect ratio, and successive refinements were compared using predicted head and hydraulic efficiency. The final mesh was accepted when the change between consecutive meshes fell

within the study tolerance; the corresponding mesh characteristics and near-wall resolution should be reported with the final mesh data.

2.4 CFD simulation

Steady-state simulations were performed in ANSYS CFX using an inlet mass flow rate of 44.9 kg/s and an outlet static pressure of 91 bar. Liquid hydrogen properties, including density, viscosity, and compressibility, were specified as temperature-dependent values based on Table 1. Turbulence was represented with the k–ω SST model, and the rotating and stationary domains were coupled through the selected frame-change/interface treatment. The solution was considered converged when residuals and monitored hydraulic quantities stabilized.

2.5 One-way fluid–structure interaction and structural analysis

The converged CFD pressure and temperature fields were mapped onto the structural finite element model in ANSYS Mechanical. This was a one-way coupling: fluid loads were transferred to the structure, but structural deformation was not fed back into the flow solution. The impeller was constrained at the shaft interface, and the rotational speed of 35,800 rpm was applied to capture centrifugal loading. The mapped thermal field was included with the pressure loading. The structural analysis returned the maximum von Mises stress and total deformation for each material configuration.

2.6 Modal analysis

Modal analysis was used to extract the first six natural frequencies and corresponding mode shapes for each material configuration. These frequencies were compared with the approximately 597 Hz operating frequency and its relevant harmonics to identify potential resonance margins.

2.7 Material selection and assessment

Inconel 718 was used as the baseline cryogenic impeller material. Six alternatives were assessed: $Al_{0.5}CoCrFeMnNi$, $Al_{0.1}CoCrFeNi$, $Al_{0.3}CoCrFeNi$, CoCrFeMnNi, Al6061 reinforced with 5 wt% B_4C, and Al6061 reinforced with 5 wt% SiC. Temperature-dependent cryogenic properties were applied in the structural and modal simulations. The materials were compared using stress, deformation, natural-frequency margin, density-related weight implications, and the available evidence on cryogenic toughness and hydrogen embrittlement.

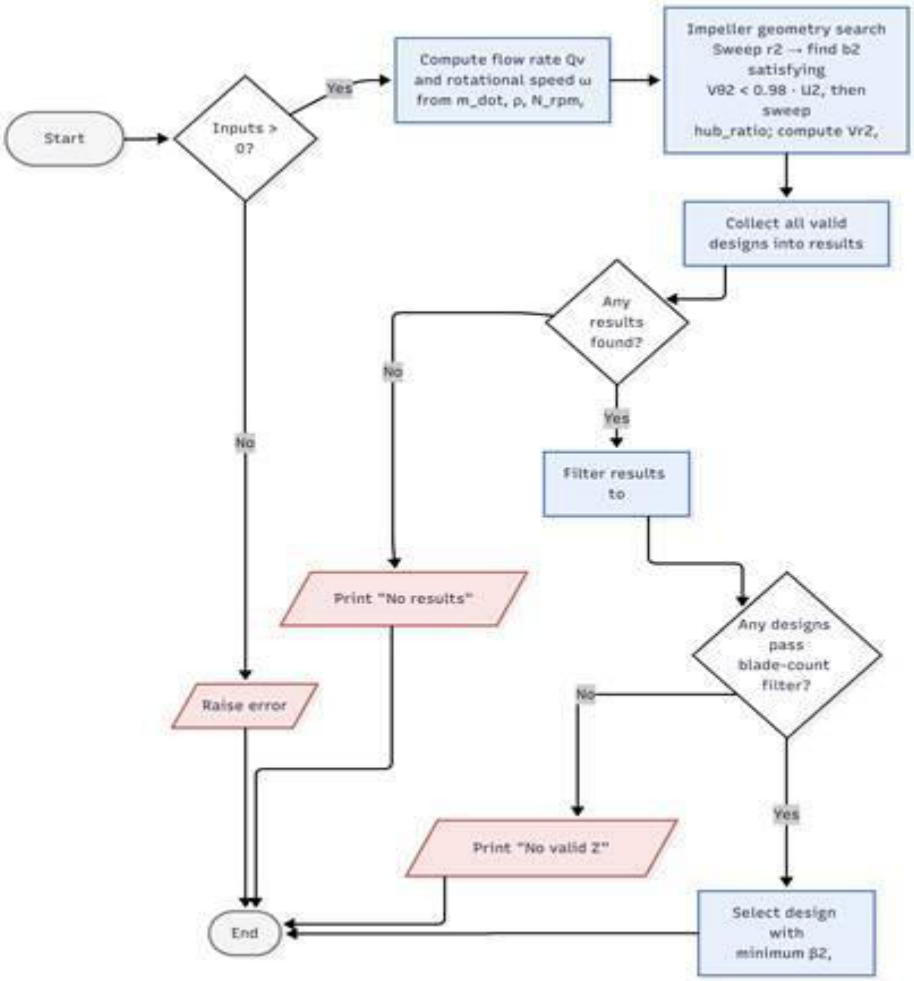


Figure 2 Algorithm flowchart for blade geometry generation

3. Implementation

3.1 Parametric Blade Geometry Generation

The in-house Python code generated candidate impeller geometries from the specified mass flow rate, LH_2 density, rotational speed, and per-stage pressure rise. It calculated the corresponding volumetric flow rate and angular velocity internally, then evaluated each candidate using the velocity triangle, outlet flow angle, blade chord, thickness, leading-edge radius, and blade count. No governing equation is required in this subsection because the implementation is described through the input variables, design constraints, and output parameters.

The code performed nested sweeps over tip radius r_2, blade height b_2, and hub-to-tip ratio. The 45 candidates were screened for a blade count between four and eight and ranked by outlet blade angle. The selected configuration met the pressure-rise requirement while retaining a

feasible velocity triangle and a practical blade geometry. The resulting parameters were exported to ANSYS BladeGen for three-dimensional construction.

3.2 ANSYS Simulation Setup

3.2 1 Geometry Generation in ANSYS BladeGen

The selected blade parameters were imported into ANSYS BladeGen to construct the complete three-dimensional impeller. Blade profiles were interpolated between the hub and shroud, and smooth leading- and trailing-edge transitions were applied to reduce geometric stress concentrations. The resulting model was used consistently in the CFD, FSI, and modal analyses, as shown in Figure 3.



Figure 3 ANSYS workflow for CFD, FSI, and modal analysis

3.2.2 Meshing in ANSYS TurboGrid

The three-dimensional impeller was meshed in ANSYS TurboGrid with a structured hexahedral topology and refined near-wall regions. The mesh was refined successively while monitoring outlet pressure and hydraulic efficiency. The final mesh was selected once the change in the monitored quantities was within the study tolerance, providing the mesh used for the CFX, FSI, and modal results reported in Section 4.

3.2.3 CFD Analysis in ANSYS CFX

The final mesh was imported into ANSYS CFX for a steady-state simulation at the design operating point. The inlet mass flow rate was 44.9 kg/s and the outlet static pressure was 91 bar. Liquid hydrogen was modelled using the temperature-dependent properties listed in Table 1. The CFX solution supplied the pressure, velocity, and temperature fields used as loads in the one-way FSI analysis. The resulting pressure rise and efficiency are reported in Table 3.

The properties were specified for liquid hydrogen, including temperature-dependent density and viscosity. Results from CFD simulations provided the distribution of velocities, pressure, and temperature data that served as structural loading for the FSI analysis.

3.2.4 Fluid-Structure Interaction (FSI) in ANSYS Mechanical

For the one-way FSI analysis, the impeller was constrained at the shaft interface, and the mapped CFD pressures and temperatures were applied together with the 35,800-rpm rotational load. The structural solution returned the maximum von Mises stress and total deformation for each material. These values are compared in Table 4.

3.2.5 Modal and Dynamic Analysis

Modal analyses were performed for each material configuration to obtain the first six natural frequencies and their mode shapes. The frequencies were compared with the 597 Hz shaft operating frequency and considered alongside relevant harmonics. Table 5 summarizes the resulting dynamic response.

3.2.6 Material Comparisons

The material comparison included the Inconel 718 baseline, four HEAs, and two Al6061-based composites reinforced with 5 wt% B_4C or 5 wt% SiC. The same geometry, loading conditions, and analysis sequence were used for each material so that differences in stress, deformation, and natural frequency could be compared directly.

4. Results and Discussion

Table 3. CFX pressure and efficiency results

Quantity	Design target	CFX result
Outlet pressure	91.0 bar	91.2 bar
Hydraulic efficiency	—	0.9386

Table 4 FSI stress and deformation results

Material	**Max Stress (MPa)**	**Deformation(m)**
Inconel 718	158	.0001088
$Al_{0.1}CoCrFeNi$	161	.0001085
$Al_{0.3}CoCrFeNi$	159	.0001084

$Al_{0.5}CoCrFeMnNi$	162	.0001084
CoCrFeMnNi	164	.0001084
Al6061 + 5 wt% B_4C	119	.0001145
Al6061 + 5 wt% SiC	118	.0001151

Table 5. First six natural frequencies for each material

Material	Mode 1	Mode 2	Mode 3	Mode 4	Mode 5	Mode 6
Inconel 718	959.88	1049.8	2654.4	3204.3	4867.9	7954.2
$Al_{0.1}CoCrFeNi$	951.24	1051.5	2660.5	3209.9	4880.9	7974.6
$Al_{0.3}CoCrFeNi$	961.78	1052.1	2660.5	3212.8	4885.3	7985.1
$Al_{0.5}CoCrFeMnNi$	961.52	1051.9	2661.9	3210.9	4884	7979.5
CoCrFeMnNi	961.24	1051.6	2662.4	3209.3	4881.9	7973.3
Al6061 + 5 wt% B_4C	956.25	1039.2	2581.2	3203.7	4791.3	7889.2
Al6061 + 5 wt% SiC	954.43	1036.6	2568.9	3195.9	4772.8	7864.9

The CFD solution reached an outlet pressure of 91.2 bar against the 91 bar design target, a difference of approximately 0.2%. The hydraulic efficiency was 0.9386. These values indicate that the selected geometry met the intended single-stage duty point with low predicted hydraulic losses. The pressure and efficiency results are summarized in Table 3.

The FSI results in Table 4 show that the maximum von Mises stress ranged from 118 to 164 MPa across the seven materials. Inconel 718 reached 158 MPa, while CoCrFeMnNi reached the highest value at 164 MPa. The Al6061 + 5 wt% SiC composite produced the lowest stress, 118 MPa, and the Al6061 + 5 wt% B_4C composite produced 119 MPa. The smallest deformations were obtained for the HEA configurations, at approximately 1.084×10^{-4} m, whereas the aluminium composites showed slightly larger deformations. Thus, the composites reduced stress, while the HEAs provided the best deformation response in this model.

All seven material configurations remained within the elastic limits assigned in the structural model. This is a computational screening result rather than an experimental qualification: the conclusion depends on the cryogenic material properties and boundary conditions used in the simulation. The stress and deformation trends nevertheless provide a consistent basis for comparing the candidates.

The modal results in Table 5 cover the first six modes for each material. The first natural frequencies lie between approximately 951 and 962 Hz, above the 597 Hz shaft frequency. The

higher modes extend to about 7,865–7,985 Hz. None of the reported modes coincides with the operating frequency, providing a first-pass resonance margin; a complete rotor-dynamic assessment would still need to examine shaft flexibility, blade-passing excitation, damping, and higher harmonics.

Taken together, the CFD, FSI, and modal results show that the selected impeller met the pressure target while maintaining acceptable stresses and separation between the operating frequency and the first six computed modes. Because no experimental pump data were available in the supplied study, validation is limited to agreement with the specified Vulcain 2 design point, internal mesh/convergence checks, and consistency between the hydraulic, structural, and dynamic outputs. Experimental cryogenic testing remains necessary before any material can be treated as flight qualified.

5. Conclusion

- The computational workflow produced a single-stage LH_2 impeller design that reached an outlet pressure of 91.2 bar at a hydraulic efficiency of 0.9386 for the specified 44.9 kg/s and 35,800 rpm operating point.
- One-way FSI and modal analyses showed that all seven candidate materials remained within the elastic limits used in the model, while the first six natural frequencies remained above the 597 Hz shaft operating frequency.
- The Al6061 + 5 wt% SiC composite produced the lowest maximum stress, 118 MPa, while the HEA configurations produced the smallest computed deformations, approximately 1.084×10^{-4} m.
- CoCrFeMnNi and the SiC-reinforced Al6061 composite are promising candidates for further cryogenic turbomachinery studies, but their performance must be confirmed through fatigue, hydrogen-exposure, manufacturing, and cryogenic testing.
- The results support the use of lower-density material systems as a route toward reducing centrifugal loading in cryogenic turbopumps, while also showing that computational screening cannot replace experimental qualification.

Funding: This research received no specific grant from any funding agency in the public, commercial, or non–profit sectors.

Declaration: Ethics, Consent to Participate, and Consent to Publish are not applicable.

Data availability statement: The article contains all of the evidence that backs up the study's conclusions.

References

[1] D. Bauer, "Copyright© 2022 by Turbomachinery Laboratory, Texas A&M Engineering Experiment Station Additive Manufacturing of Cryogenic Pump Impellers," 2022.

[2] J. Bird *et al.*, "Cryogenic pumping of liquid hydrogen for aerospace propulsion," *Progress in Aerospace Sciences*, vol. 160, p. 101155, Jan. 2026, doi: 10.1016/j.paerosci.2025.101155.

[3] M. L. Huber, E. W. Lemmon, I. H. Bell, and M. O. McLinden, "The NIST REFPROP Database for Highly Accurate Properties of Industrially Important Fluids," *Ind. Eng. Chem. Res.*, vol. 61, no. 42, pp. 15449–15472, Oct. 2022, doi: 10.1021/acs.iecr.2c01427.

[4] W. N. Hall, P. Hildebrand, and Q. D. S. Ko, "LIQUID HYDROGEN PUMP," 1964.

[5] Y. Wan, M. Manfredi, A. Pasini, and Z. Spakovszky, "Dynamic Model-Based Identification of Cavitation Compliance and Mass Flow Gain Factor in Rocket Engine Turbopump Inducers," *J. Eng. Gas Turbines. Power*, vol. 143, no. 2, Feb. 2021, doi: 10.1115/1.4049015.

[6] X. Bu, P. Fu, H. Cong, and Z. Sun, "Influence of Rotating Speeds and Thermodynamic Effects on LOX Turbopump Performance," *International Journal of Aerospace Engineering*, vol. 2023, pp. 1–22, Apr. 2023, doi: 10.1155/2023/7687760.

[7] K. Cui, P. K. Liaw, and Y. Zhang, "Cryogenic-Mechanical Properties and Applications of Multiple-Basis-Element Alloys," Dec. 01, 2022, *MDPI*. doi: 10.3390/met12122075.

[8] Y. Cui, L. Wang, and J. Ren, "Multi-functional SiC/Al composites for aerospace applications," *Chinese Journal of Aeronautics*, vol. 21, no. 6, pp. 578–584, 2008, doi: 10.1016/S1000-9361(08)60177-6.

[9] W. N. Hall, P. Hildebrand, and Q. D. S. Ko, "LIQUID HYDROGEN PUMP," 1964.

[10] A. Minick and S. Peery, "Design and development of an advanced liquid hydrogen turbopump," in *34th AIAA/ASME/SAE/ASEE Joint Propulsion Conference and Exhibit*, Reston, Virginia: American Institute of Aeronautics and Astronautics, Jul. 1998. doi: 10.2514/6.1998-3681.

[11] Y. Demyanenko *et al.*, "Single-Shaft Turbopumps in Liquid Rocket Engines," 2006.

[12] H. Dieringa, "Influence of cryogenic temperatures on the microstructure and mechanical properties of magnesium alloys: A review," Feb. 01, 2017, *MDPI AG*. doi: 10.3390/met7020038.

[13] M. Gao *et al.*, "Enhanced strength-ductility synergy in a boron carbide reinforced aluminum matrix composite at 77 K," *J. Alloys Compd.*, vol. 818, p. 153310, Mar. 2020, doi: 10.1016/j.jallcom.2019.153310.

[14] X. Gao *et al.*, "High-entropy alloys: a review of mechanical properties and deformation mechanisms at cryogenic temperatures," *J. Mater. Sci.*, vol. 57, no. 12, pp. 6573–6606, Mar. 2022, doi: 10.1007/s10853-022-07066-2.

[15] Y. H. Jo *et al.*, "Analysis of damage tolerance of TRIP-assisted V10Cr10Fe45Co30Ni5 high-entropy alloy at room and cryogenic temperatures," *J. Alloys Compd.*, vol. 844, p. 156090, Dec. 2020, doi: 10.1016/j.jallcom.2020.156090.

[16] M. Reytier, "Characterization of titanium alloys for cryogenic applications," in *AIP Conference Proceedings*, AIP, 2002, pp. 76–83. doi: 10.1063/1.1472528.

[17] J. M. Park *et al.*, "Role of BCC phase on tensile behavior of dual-phase Al0.5CoCrFeMnNi high-entropy alloy at cryogenic temperature," *Materials Science and Engineering: A*, vol. 746, pp. 443–447, Feb. 2019, doi: 10.1016/j.msea.2019.01.041.

[18] K. KAMIJO, E. SOGAME, and A. OKAYASU, “The development of small liquid oxygen and liquid hydrogen turbopumps of a LE-5 rocket engine,” in *17th Joint Propulsion Conference*, Reston, Virigina: American Institute of Aeronautics and Astronautics, Jul. 1981. doi: 10.2514/6.1981-1375.

[19] N. Koga, T. Nameki, O. Umezawa, V. Tschan, and K.-P. Weiss, “Tensile properties and deformation behavior of ferrite and austenite duplex stainless steel at cryogenic temperatures,” *Materials Science and Engineering: A*, vol. 801, p. 140442, Jan. 2021, doi: 10.1016/j.msea.2020.140442.

[20] N. Nayan *et al.*, “Mechanical properties of aluminium–copper–lithium alloy AA2195 at cryogenic temperatures,” *Mater. Des.*, vol. 58, pp. 445–450, Jun. 2014, doi: 10.1016/j.matdes.2014.02.024.

[21] S. Trivedi, H. Sen, and P. Kumar Das, “Design of Centrifugal Pumps with Non-Overloading Power Curve: A Review of the State of the Art,” *Cureus Journal of Engineering*, Feb. 2025, doi: 10.7759/s44388-024-00561-z.

[22] A.-C. Cancescu, D.-E. Crunteanu, A.-M. T. Andreescu, S.-N. Danescu, and V. Dragan, “Hydraulic Design of an Ultracompact Liquid Methane–Liquid Oxygen Turbopump for a Mid-Scale Thruster for Upper Stage Application,” *Inventions*, vol. 9, no. 5, p. 104, Sep. 2024, doi: 10.3390/inventions9050104.

[23] G. Peng, Q. Chen, L. Zhou, B. Pan, and Y. Zhu, “Effect of Blade Outlet Angle on the Flow Field and Preventing Overload in a Centrifugal Pump,” *Micromachines (Basel).*, vol. 11, no. 9, p. 811, Aug. 2020, doi: 10.3390/mi11090811.

[24] X. Han, Y. Kang, D. Li, and W. Zhao, “Impeller Optimized Design of the Centrifugal Pump: A Numerical and Experimental Investigation,” *Energies (Basel).*, vol. 11, no. 6, p. 1444, Jun. 2018, doi: 10.3390/en11061444.

[25] R. Bosson, P. Sabin, and G. Turin, “Improvements of the hydrogen turbopump for the Vulcain 2 engine,” in *35th Joint Propulsion Conference and Exhibit*, Reston, Virigina: American Institute of Aeronautics and Astronautics, Jun. 1999. doi: 10.2514/6.1999-2344.